Rigid Deployable Solar Array

A.M. Watt and S. Pellegrino

CUED/D-STRUCT/TR214

Department of Engineering
University of Cambridge

Release date: 7 July, 2004.

Summary

This report is concerned with the design of low-cost rigid-panel deployable solar arrays with self-locking tape-spring hinges. The report presents a detailed study of the behaviour of the hinges, involving both finite-element simulations and direct experimental measurements. It also presents a validation of the analytical model recently proposed by Schultheiss, through comparisons with simulations with a Pro/Mechanica model. An analysis of the effects of misalignment of the gravity compensations system is carried out. Finally, the effects of air drag on the deployment of a solar array wing are evaluated experimentally.

Contents

List of Figures

Chapter 1

Introduction

This report is concerned with the design of low-cost rigid-panel deployable solar arrays that use self-locking tape-spring hinges to connect the panels. Because these hinges have practically no stiffness when they are folded, great care is required when their deployment is carried out under gravity conditions.

A simple and yet effective gravity compensation scheme for a solar array wing consisting of two panels and a yoke has been presented by Schultheiss (2003). This proposed design relies on the tape-spring hinges deploying both the solar-array wing and the movable parts of the gravity compensation system. An important characteristic of this approach is that the mass distribution and friction in the offload system affect the deployment behaviour that is then observed. However, these effects can be accurately quantified, and hence can be included in the model of the array. Thus, by validating experimentally —under gravity— an analytical model of the combined system formed by the array and the gravity compensation system —whose components have been accurately characterised— it is possible to validate also the model of the array deploying in gravity-free conditions.

This report tackles some of the detailed issues that follow on from Schultheiss work. Three important issues are studied, as follows.

- The behaviour of the hinges, studied by means of finite-element simulations and also through direct experimental measurements.
- Validation of the analytical model proposed by Schultheiss (2003), through comparisons with simulations with a Pro/Mechanica model, and analysis of the effects of misalignment in the gravity compensation system.
- Evaluation of air effects on the deployment of a solar array wing.

1.1 Layout of Report

This report is presented in five chapters.

Following this introduction, Chapter 2 presents finite-element simulations of a panel-panel hinge and of the root hinge, which are compared with experimental results. A simple design method for the preliminary design of the root hinge is also presented.

Chapter 3 presents a revised simulation of the deployment of the same solar array wing mock-up described in Chapter 4 of Schultheiss (2003), using the simulation software developed by Schultheiss, but using a more accurate description of the moment-rotation profile for the hinges. Analyses of the sensitivity of the hinge latching times to friction in the trolleys of the gravity offload system, and horizontality of the longitudinal tubes of the offload are presented. An alternative simulation technique, using Pro/Mechanica, is then presented and —as this model includes the elastic compliance of the hinges— estimates of the maximum latching moments in the root hinge are obtained.

Chapter 4 presents an experimental study of the effects of air drag on the panels, showing that these effects are quite small.

Chapter 5 concludes the report.

Chapter 2

Hinge Moment-Rotation Relationship

2.1 Panel-Panel Hinge

The hinge between the panels consists of four tape-springs arranged as shown in Figure 2.1. The tape-springs have a separation, s, measured as the distance between the innner surfaces of the tape-springs, which is 25 mm.

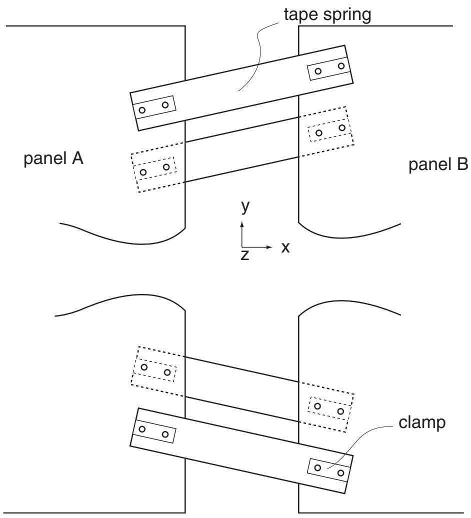

Figure 2.1: Coordinate system used in FE model for panel-panel hinge.

2.1.1 Modelling of Panel-Panel Hinge

A full three-dimensional model of the tape-spring hinge, Figures 2.2 and 2.3, was built using Abaqus 6.3 (ABAQUS 2002). A pair of tape-springs was modelled using 4-node doubly curved general-purpose shell elements (s4), with 600 elements (corresponding to a 50 × 12 mesh) representing each tape-spring. These shell elements were generated with logarithmic bias along the tape length so that the mesh is much finer in the middle, where the largest curvatures are achieved.

The global coordinate system for the analysis is defined in Figure 2.1, however the two tape-springs were located above one another in the model, as this allowed a previous finite-element model to be used with minimal modification.

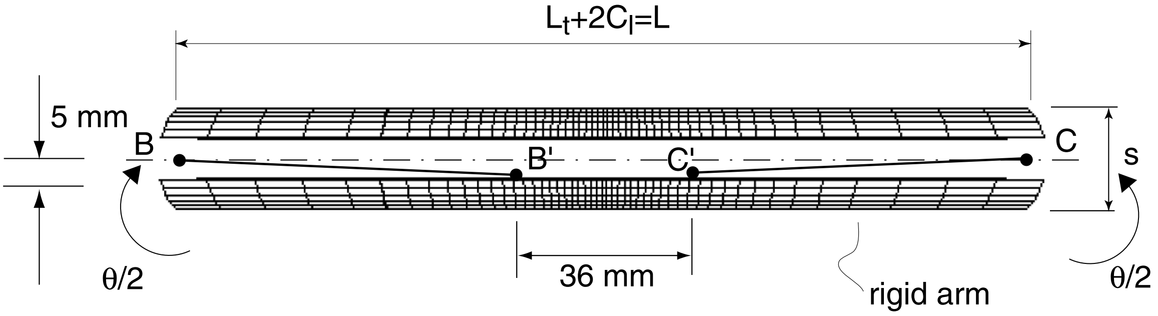

Figure 2.2: Finite element model of panel-panel tape-spring hinge (side view).

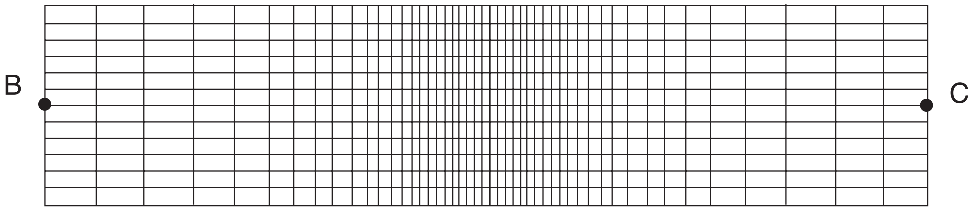

Figure 2.3: Finite element model of panel-panel tape-spring hinge (top view).

The ends of the tape springs are held under rigid clamps. Hence, the finite-element mesh at the end of the tapes has to be arranged such that the clamped area corresponds to an integer number of elements and the nodes of these elements lie exactly on the boundary of the clamp, as shown in Figure 2.4. Note that C_b and C_l are the width (8 mm) and length (21 mm) of the clamp, respectively.

The nodes under the clamps, Figure 2.4, are kinematically fully coupled to nodes B and C, which lie halfway between the tape-springs, see Figure 2.2. Nodes B and C are in turn rigidly connected to nodes B' and C', which are located 5 mm below the mid-plane of the hinge, and at a distance of 36 mm from one another. These distances are chosen such that when nodes B' and C' are rotated through 90° about the y-axis, in the directions shown in Figure 2.2, nodes B and C end up at a distance of 26 mm. This is the distance between the mid-planes of the panels of the solar array, in the folded configuration, that is envisaged in the current SSTL design.

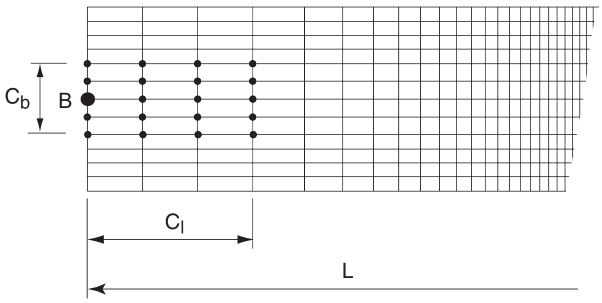

Figure 2.4: Nodes under the clamp.

Nodes B' and C' are fixed against translation in all directions and against rotation about the x and z axes. In order to fold the hinge, clockwise and anti-clockwise rotations of up to 90° are applied to nodes B' and C', respectively.

The finite-element analysis proceeds in two steps:

1. Folding step. This gets the tape-spring into the correct folded configuration. This involves rotating nodes B' and C' through $+90°$ and $-90°$, around the y-axis.

2. Unfolding step. In this step the translational constraint in the x-direction on node C' is removed, and B' and C' are rotated through equal amounts until the hinge has fully deployed.

The deployment moment for the complete panel-panel hinge, i.e. including four tape-springs in total between the panels, can be seen in Figure 2.5. The close-up in Figure 2.6 shows more clearly the moment response for large scale rotations. These results give the moment about the y-direction, obtained from the simulation described above, multiplied by two. Moments about axes other than the y-axis have been ignored as these are balanced by equal and opposite moments from the other pair of tape springs.

It can be seen that, for the complete panel-panel hinge set-up, the buckling moment is approximately 11 Nm and the deployment moment is approximately 200 Nmm. The initial stiffness is approximately 2.29 kNm/rad, as can be seen from Figure 2.7. The maximum Mises stress in the tape-springs is 2036 N/mm^2, occurring in the fully folded position.

The folded configuration of a two-tape spring hinge, where the tape springs are one above the other for simplicity, as explained earlier, can be seen in Figure 2.8. Note that the tape springs are allowed to go through one another in this model, as in reality they would be offset in the y-direction, and so no interference would occur.

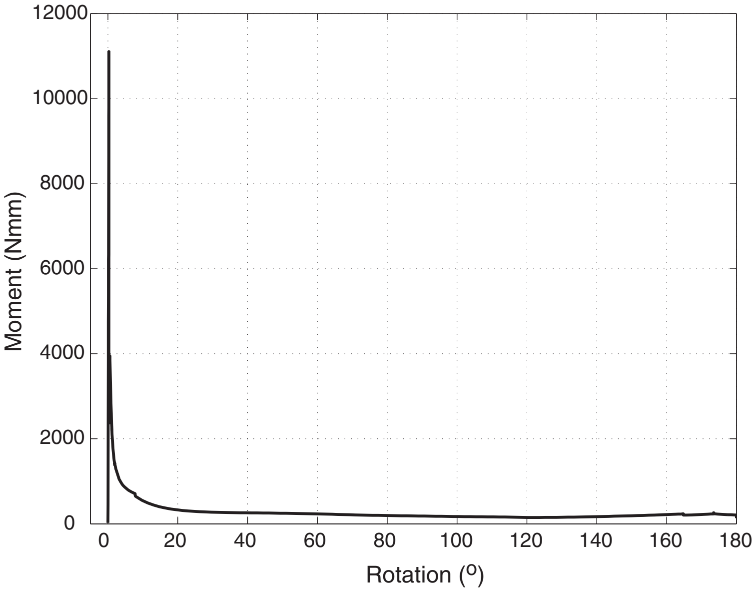

Figure 2.5: Moment-rotation properties of panel-panel hinge.

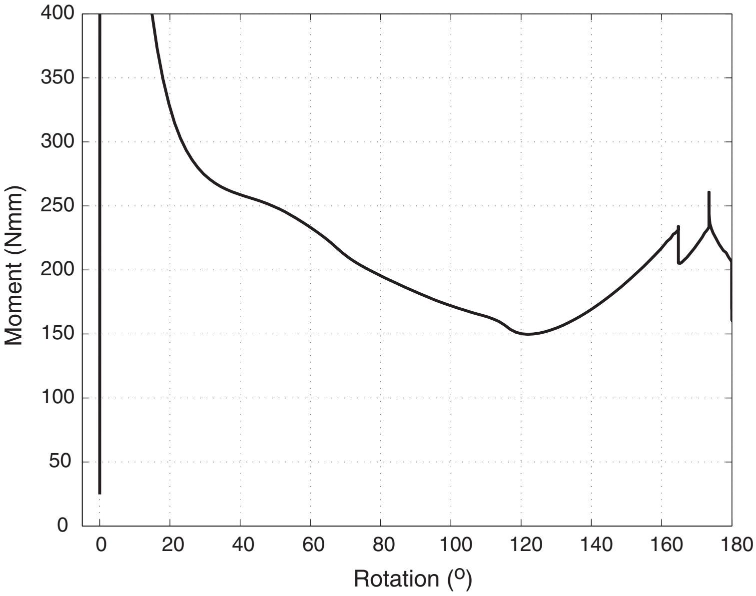

Figure 2.6: Moment-rotation properties of panel-panel hinge (close-up)

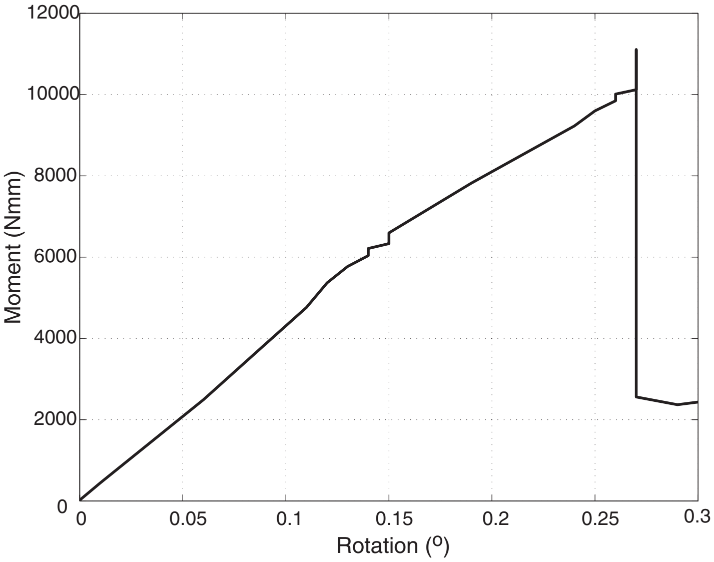

Figure 2.7: Moment-rotation properties of panel-panel hinge, showing initial stiffness.

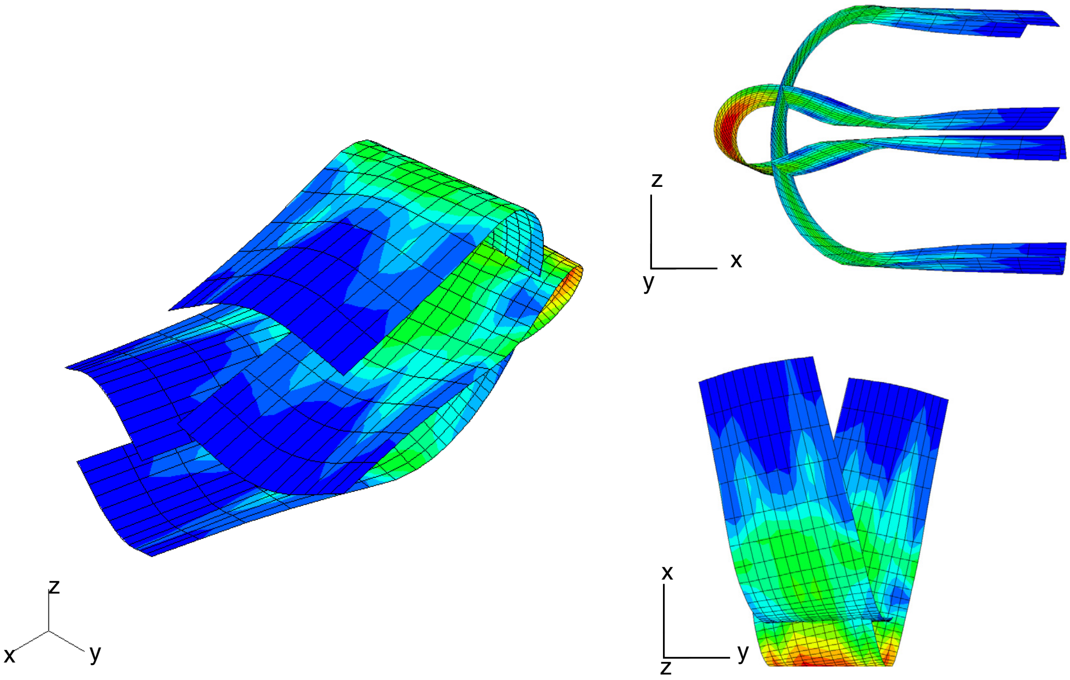

Figure 2.8: Three views of panel-panel tape-spring hinge, in folded configuration.

2.1.2 Limitations of Panel-Panel Hinge Model

The finite element model of the tape-spring assumes deployment to be a quasi-static process. A full dynamic model could be used, but the inertias of the panels would have to be included in the model, which would increase its complexity impractically. Inertia would add extra constraints on the tape-spring, which have not been included in the present model, in essence making the tape-spring deploy in a slightly different manner to that predicted here. Givois et al. (2001) faced a similar problem in their design of a tape-spring hinge and found that the effects of the panel inertias did not change the deployment of the tape-springs significantly.

2.1.3 Experimental Measurement of Moment-Rotation Relationship

The moment-rotation relationship of a panel-panel hinge during deployment was measured by connecting four tape-springs, arranged in a configuration equivalent to that used in the panel-panel hinges, to two specially made end connectors. These end connectors were connected to a rig (Fischer 1995) that allows the two connectors to be rotated about the z-axis, while allowing free translation in the x-direction of one end connector, Figure 2.9. The moment applied to each connector is measured by means of strain gauges attached to hollow shafts that support the connectors.

The test procedure was as follows:

1. Set rotation of one side of the hinge.
2. Adjust rotation of the other side until the moments on both sides are approximately equal.
3. Read moment and rotation values.
4. Repeat for new rotation.

The measurements from two nominally identical tests, both beginning with the rotation set at 180°, are shown by means of solid lines in Figure 2.10. Note that, apart from small deviations in the value of the rotation at which there are relatively large variations in the moment, the two tests produced almost identical results.

In the experiments, the tape-spring hinge could not be forced into a folded configuration where its ends are very close together, as it is envisaged for the packaged configuration of the SSTL solar array. Instead, it was allowed to fold into a “natural”, lower energy state. However, because the earlier finite-element simulation had forced the hinge into a higher-energy state, a

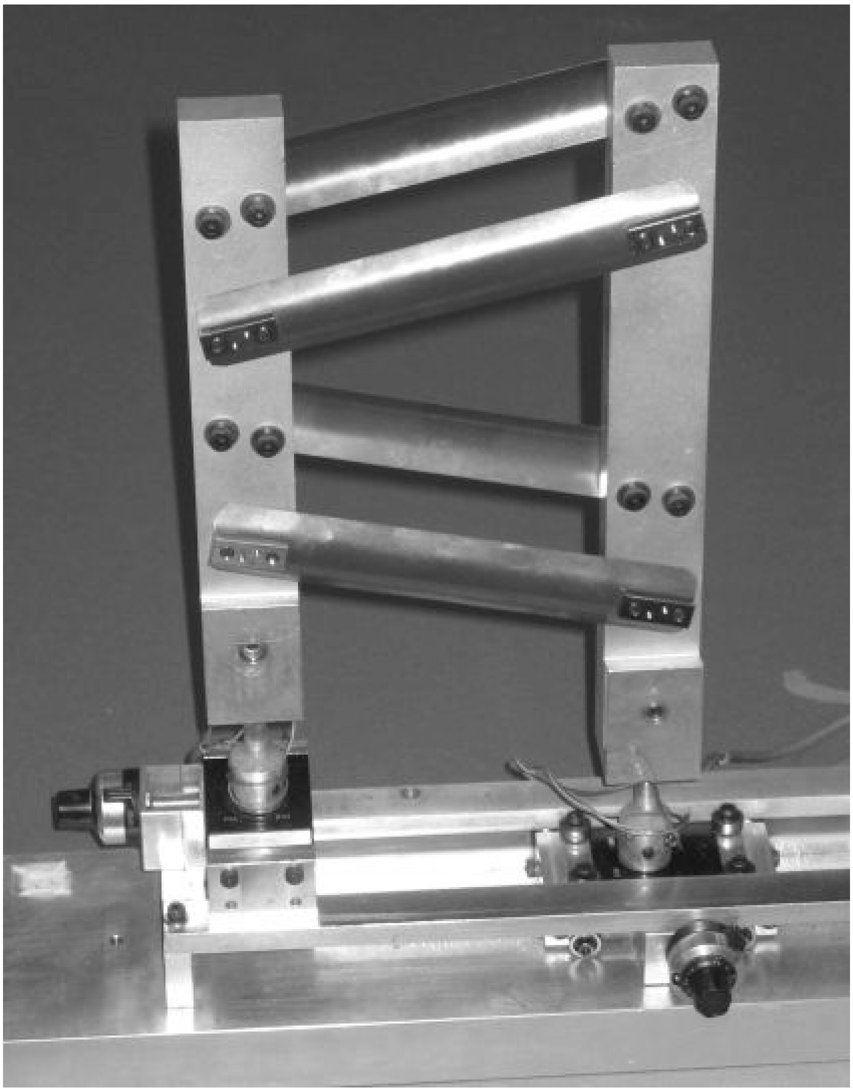

Figure 2.9: Panel-panel hinge experimental set-up.

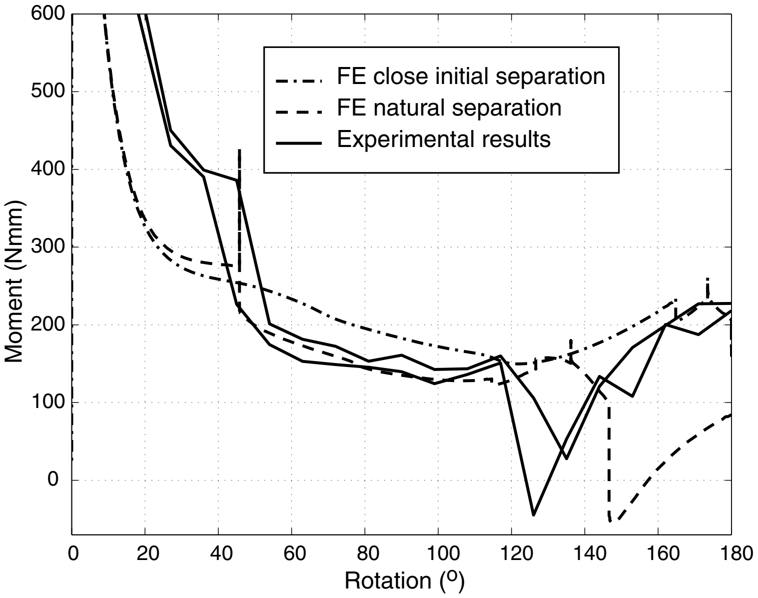

Figure 2.10: Moment-rotation relationship of panel-panel hinge.

second FE analysis was made in which translation in the x-direction of one side of the hinge was allowed during folding. The results of this analysis are shown in Figure 2.10.

It is important to compare the moment-rotation relationships obtained from the finite-element simulations of this “free” hinge vs. the constrained hinge modelled in Section 2.1.1. Note that the simulation of this “free” hinge follows closely the experimental measurements in the range 40°-180°. In both cases, the moment drops to approximately zero in the middle of this range. Somewhat surprisingly, this does not happen when the hinge is initially set with a smaller separation, in the folded configuration. It is surprising that the initial higher-strain energy state does not disappear immediately after the hinge is released. The observed behaviour suggests that the hinge, having been deformed into a higher-energy state, takes a different deployment path.

2.2 Root Hinge

The root hinge, which connects the yoke of the solar array to the solar-array drive mechanism (SADM), is a combination of a tape-spring hinge and a revolute joint.

A model of the root hinge assembly used in the deployment demonstrator (Schultheiss 2003) can be seen in Figure 2.11. The hinge consists of two U-shaped pieces connected by coaxial pins; it is designed to have up to three tape-springs, each of total length, L, of 100 mm, although in the present study only two tape-springs are used. The tape-springs are connected to the hinge body through 21 mm long connectors, giving a free tape length, L_t of 58 mm. The pins, at a distance of 14.2 mm from the top edge of the tape-spring, are housed in low-friction bushings. Engineering drawings for all the parts of this hinge can be seen in Appendix A.

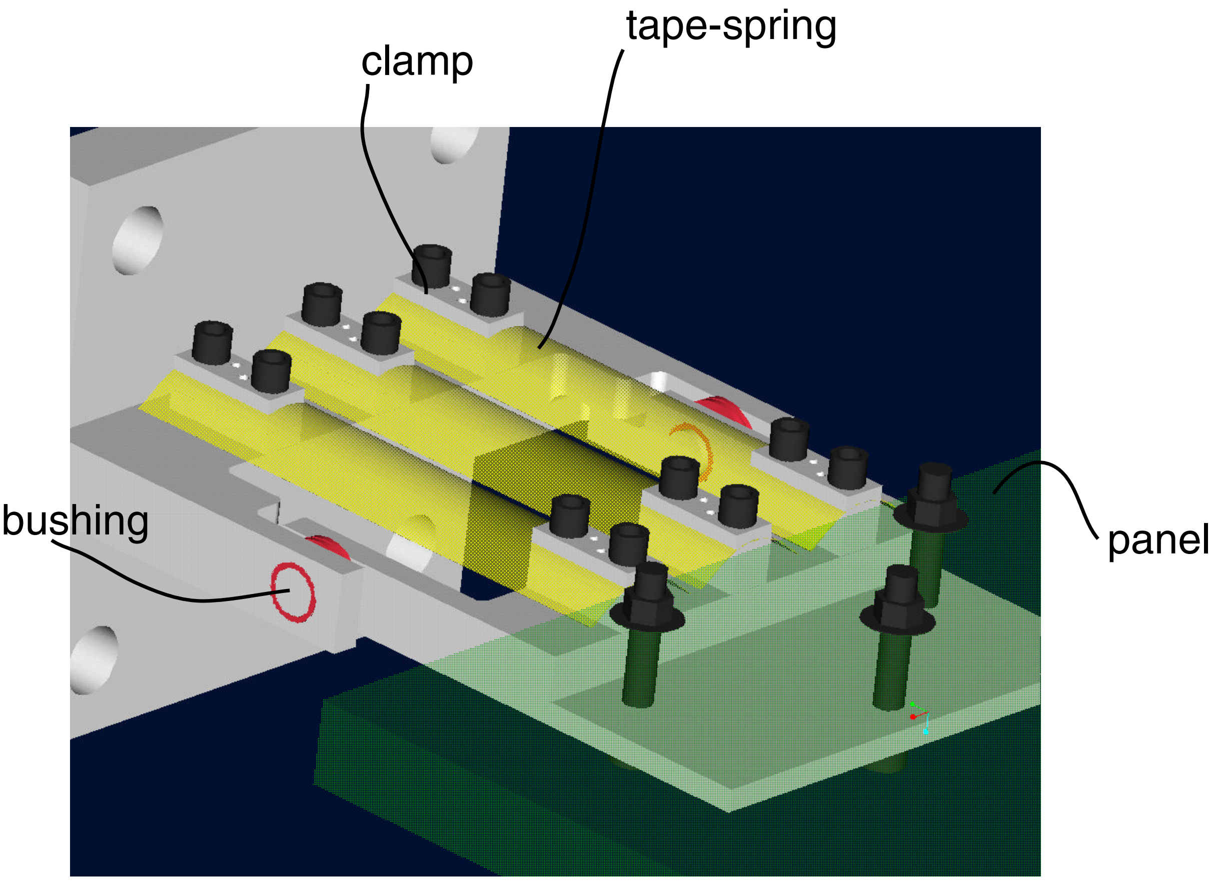

Figure 2.11: Root hinge assembly.

2.2.1 Design of Root Hinge

Two initial designs for the root hinge were proposed by SSTL; they are labelled as Designs 1 and 2 in Table 2.1. Note that the length of the clamps and the cross-sectional dimensions of the tape-springs are the same as in the panel-panel hinges.

Parameter	Symbol	Design 1	Design 2	Design 3	Units
Overall length of tape	L	70	70	90	mm
Length of clamps	L_c	21	21	20	mm
Length of free tape	L_t	28	28	50	mm
Offset from top of tape	O	14.6	10	14.6	mm

Table 2.1: Root-hinge designs.

From previous experience, it was thought that the tape-springs in these designs might be too short to prevent over-stressing during folding.

In order to check this, a very simple model of a tape-spring hinge attached to a revolute joint was made, as shown Figure 2.12. This model had the same dimensions as Design 1. It was found that the tape-spring in this hinge formed permanent creases in the middle when it was folded, and did not deploy. A longer tape-spring was then attached to the same hinge body, see Design 3 in Table 2.1. It was found that this tape-spring could be folded without forming permanent creases, although large curvatures occurred. The tape spring deployed successfully.

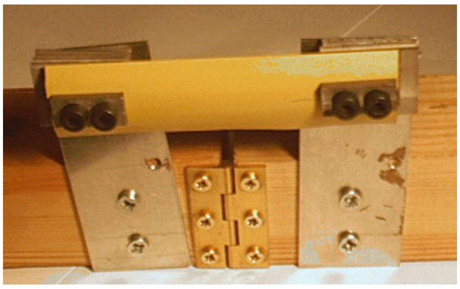

Figure 2.12: Simple model of root hinge.

A simple analysis of the curvatures induced by folding the root hinge was performed. This analysis modelled the tape-spring in the fully folded configuration (note that the maximum rotation of the root is 90°), shown in Figure 2.13, by assuming the simplified shape shown in Figure 2.14. Note that this shape assumes that the tape-spring is free to rotate at the clamps, which is incorrect, but provides a reasonable estimate of the curvature at the centre of the tape-spring, which is where creasing occurred in the real model. This assumption leads to a lower-bound estimate of the stresses induced by folding.

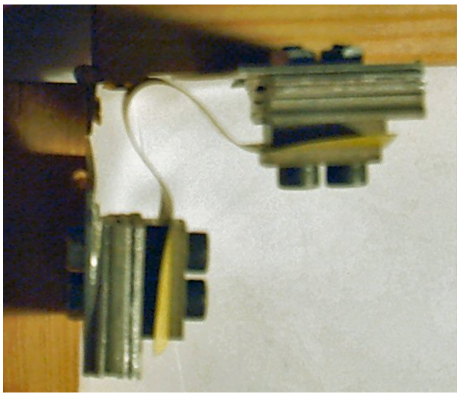

Figure 2.13: Shape of tape-spring in folded root hinge.

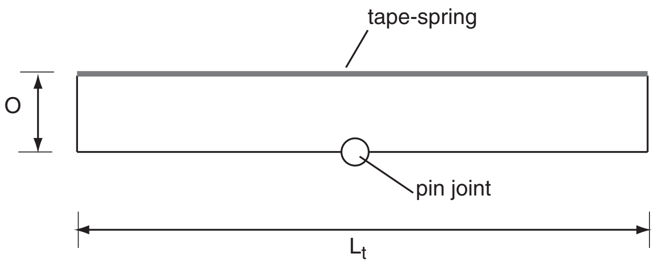

(a) Straight Position

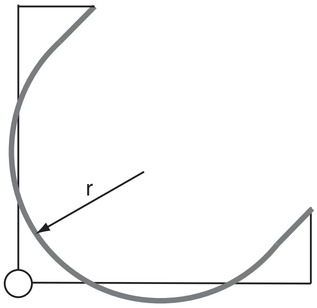

(b) Folded Position

Figure 2.14: Simplified tape-spring shape.

The radius, r, of the curved portion of the tape-spring can be then found from geometry

$$r = \frac{\sqrt{2}}{2}\left(\frac{L_t}{2} - O\right) \tag{2.1}$$

It should be noted that the maximum value of r is given by the "natural" radius of curvature of the tape-spring, which is approximately the same as R , the cross-sectional radius of the straight tape-spring (Calladine 1988). If r becomes bigger than R two separate curves joined by a straight piece would form, instead a uniformly curved piece.

The longitudinal and transverse stresses, σ_l and σ_t, induced in the top surface of the tape-spring by this enforced longitudinal curvature and the associated transverse curvature, are

$$\sigma_l = E\left(-\frac{t}{2r} + \nu\frac{t}{2R}\right) \tag{2.2}$$

$$\sigma_t = E\left(-\frac{t}{2R} + \nu\frac{t}{2r}\right) \tag{2.3}$$

Here, E is the Young's Modulus of the tape-spring, t its thickness, R its original cross-sectional radius and ν the Poisson's ratio.

Table 2.2 lists the Mises stress in tape-springs of different lengths, L_t, for root hinges whose design parameters are as listed in Table 2.3. The results in the table indicate that hinges with short tape-springs have very high stresses. Note that the yield stress for ASTM spring steel is in the range 1,590 to 2,750 N/mm^2. It can therefore be concluded that L_t should be at least 50 mm and preferably longer. The current SSTL root hinge design has a total length, L, of 100 mm corresponding to a free tape length, L_t, of 58 mm — only slightly longer than the minimum suggested length.

$L_t(mm)$	30	40	50	60	70	80
σ (N/mm^2)	49,434	2,894	1,206	741	650	650

Table 2.2: Maximum stress in tape-spring root-hinges of different lengths, L_t.

2.2.2 Finite Element Modelling of Root Hinge

A finite element model of the root hinge was set up by modifying the model of one of the tape springs used for the panel-panel hinge model. This model can be seen in Figure 2.15.

The length of the tape-spring was changed to L = 100 mm, to match the length of the current SSTL design. A uniform mesh consisting of 1 mm long elements was adopted, as the root hinge has significant curvatures both near the clamps and in the middle. This change in the mesh design resulted in a small decrease in the deployment moment, when compared with

Parameter	Value	Units
t	0.115	mm
R	13	mm
O	14.6	mm
E	210,000	N/mm^2
ν	0.3	-

Table 2.3: Design parameters of tape-spring root hinges.

initial results obtained from the logarithmic mesh used in Section 2.1.1. Further improvements in accuracy may be found by further mesh refinement. The axes were rotated about the z-axis such that the x-axis coincided with the longitudinal axis of the tape-spring, see Figure 2.15.

Rotations of $\theta/2 = +45°$ and $\theta/2 = -45°$ about the y-axis were applied to nodes B' and C', respectively. The deployment simulation run smoothly.

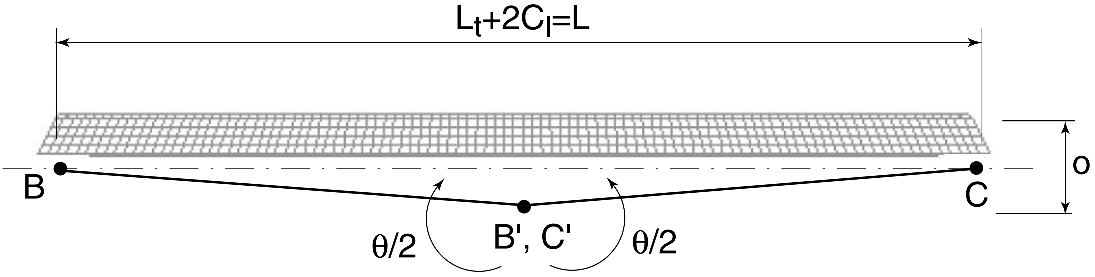

Figure 2.15: Finite element model of root hinge.

The moment-rotation relationship predicted by this analysis can be seen in Figure 2.16, with a close up —showing the deployment moment in more detail— in Figure 2.17. It should be noted that the moments have been multiplied by two, because the complete hinge has two tape-springs. The key results are as follows: the buckling moment of the hinge is 15 Nm, the deployment moment varies between 270 and 360 Nmm for most of the deployment range, and the stiffness in the deployed configuration is approximately 2000 Nm/rad.

The maximum Mises stress, ignoring any stress concentrations occurring at the clamps, is 2045 N/mm^2. This peak stress occurs when the hinge is in the fully folded position. This configuration is shown in Figure 2.19.

2.2.3 Sensitivity of Maximum Stress to Offset

To address concerns about possible damage to the tape springs due to the high stresses in the folded configuration, a preliminary study of the effect of varying the offset, O, of the tape-spring

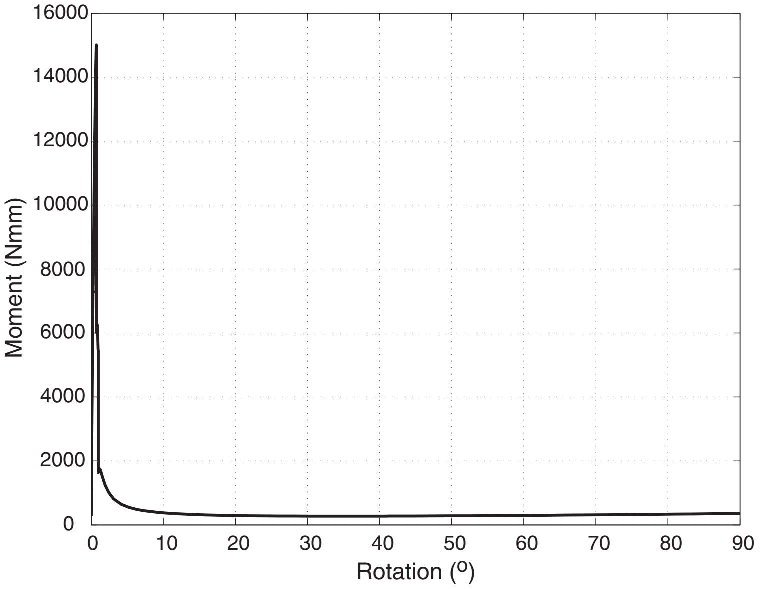

Figure 2.16: Moment-rotation properties of root hinge (full-scale).

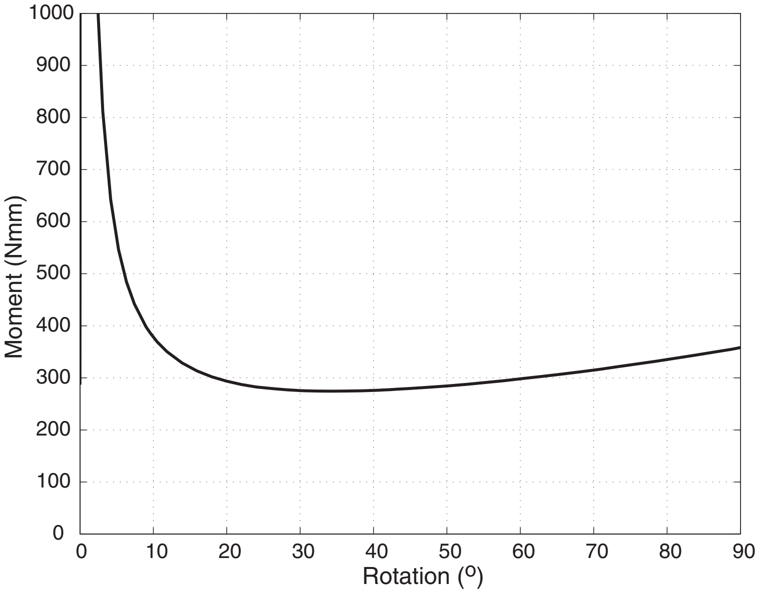

Figure 2.17: Moment-rotation properties of root hinge (close-up on deployment moment).

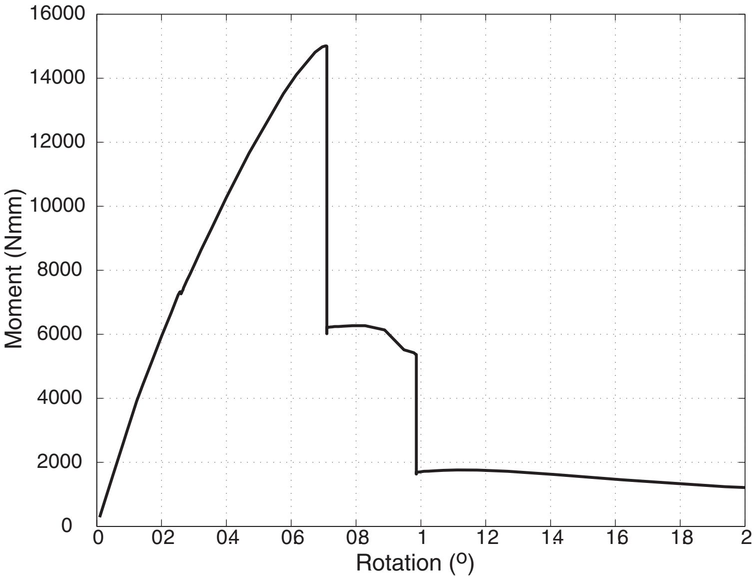

Figure 2.18: Moment-rotation properties of root hinge showing initial stiffness.

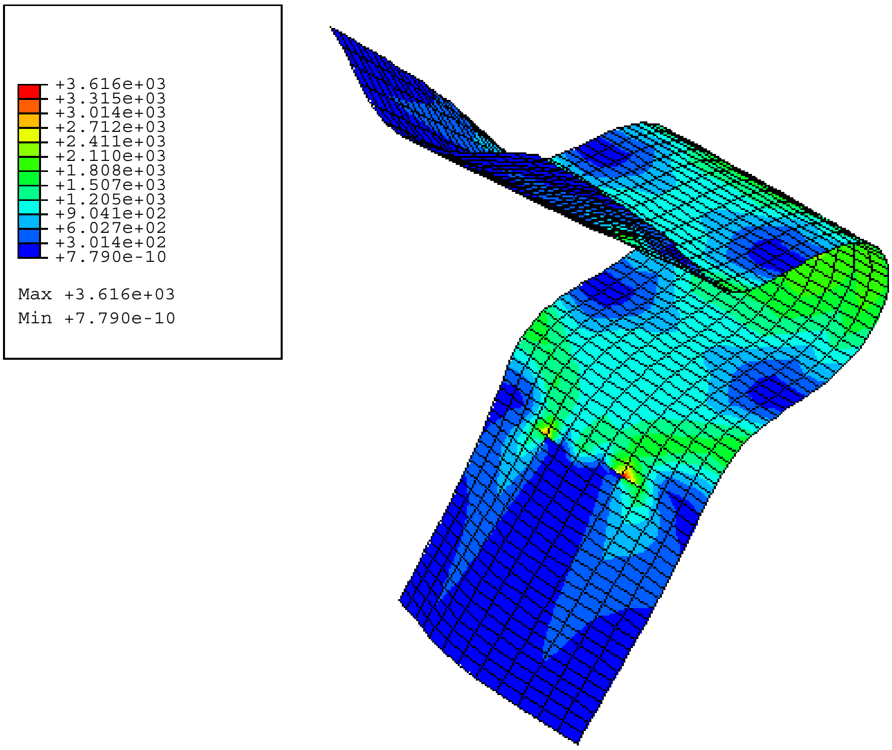

Figure 2.19: Mises stress (N/mm^2) distribution in fully folded root hinge.

in the root hinge was made. The results of this study are reported in Table 2.4. The table shows that smaller offsets lead to significant increases of the maximum stress.

Offset (mm)	Mises Stress (N/mm^2)
18.6	2935
14.6	3110
8.6	2944
4.6	3498

Table 2.4: Maximum stress in hinges with different offsets.

2.2.4 Sensitivity of Moments to Offset

Varying the offset, O, affects also the deployment moment of the root hinge, as demonstrated by Figure 2.20 which shows plots of the deployment moment for the current SSTL hinge design, with an offset of 11.8 mm, and also for hinges with offsets of 10 and 14 mm. It can be seen that the moment increases with the offset. Figure 2.21 shows that for small changes in the offset, the deployment moment (when the hinge is folded through 90°) increases approximately linearly with the offset.

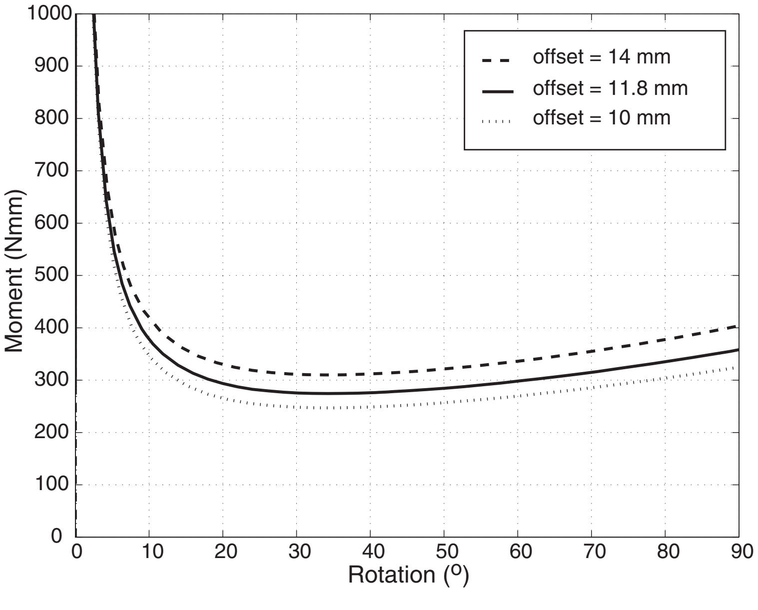

Figure 2.20: Moment-rotation relationship for different offsets.

Small changes in the offset significantly change the value of the maximum moment that can be applied to the latched hinge before the tape spring buckles. The values that correspond to the three offsets that have been investigated are listed in Table 2.5. Again, the increase is

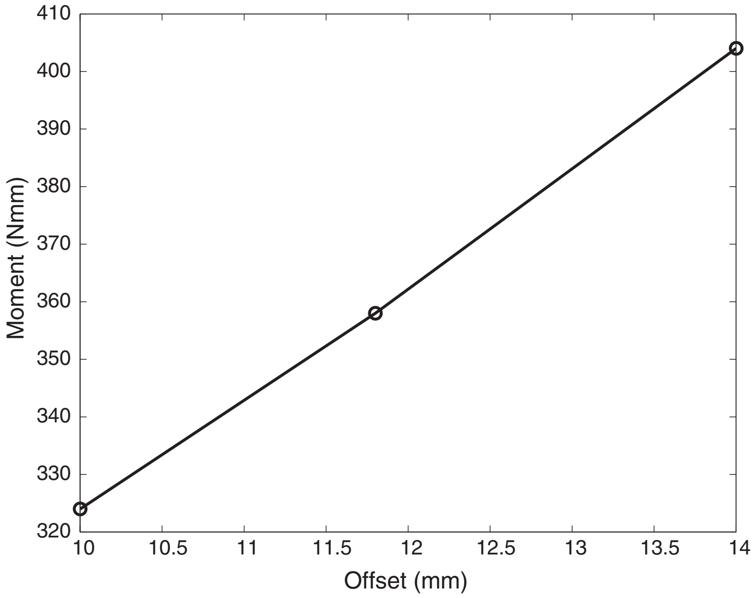

Figure 2.21: Variation of deployment moment at 90° with offset.

approximately linear with the offset, for the small range of values considered.

Offset (mm)	Moment (Nm)
14	17.6
11.8	15.0
10	12.9

Table 2.5: Variation of buckling moment with offset.

2.2.5 Experimental Measurement of Moment-Rotation Relationship

The same test rig used for measuring the behaviour of the panel-panel hinge was used also to measure the moment-rotation relationship of the root hinge. Connection pieces were fabricated to attach the root hinge to the test-rig. This set-up can be seen in Figure 2.22. The same testing procedure outlined in Section 2.1.3 was followed.

The experimental results can be seen in Figure 2.23, along with the finite element predictions for a 12 mm offset root hinge.

It can be seen that there is a discrepancy between the finite element and experimental curves, although both curves have a similar shape. The finite element results may be further improved through the use of a finer mesh.

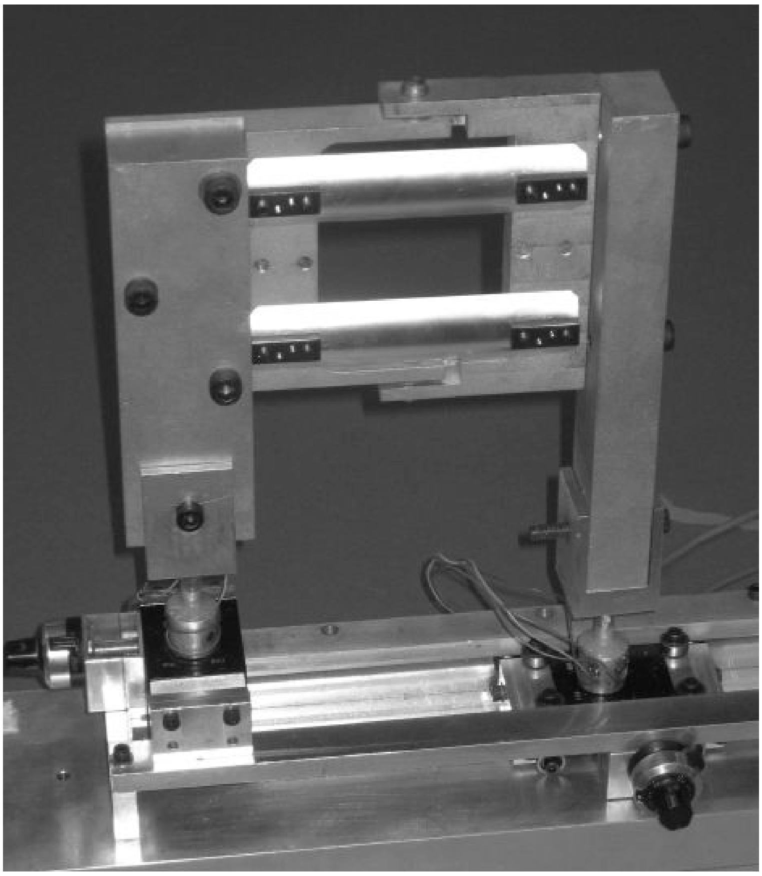

Figure 2.22: Root hinge experimental set-up.

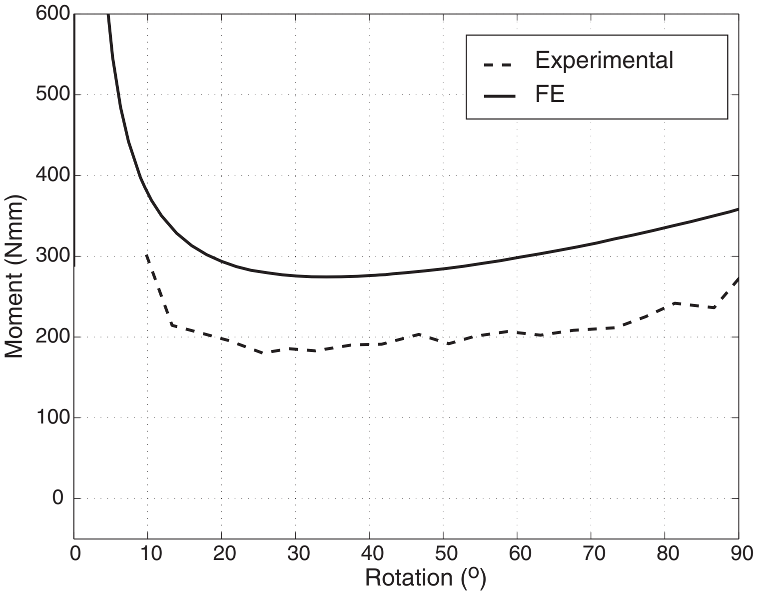

Figure 2.23: Deployment moment results for root hinge.

Chapter 3

Simulation of Deployment

Deployment of the combined system formed by the solar array wing and the gravity-offload system was simulated in two different ways. First, the Matlab simulation software written by Schultheiss was run with updated moment-rotation profiles for the hinges, based on the experimental results presented in the previous chapter. Second, a more detailed model of the system was set up in Pro/Mechanica and, after verifying that the latching times predicted by this model were consistent with those predicted by the earlier simulation, the Pro/Mechanica model was used to investigate the deployment shocks.

3.1 Revised Simulation using Schultheiss' Program

The deployment moments measured experimentally, and shown in Figures 2.10 and 2.23, were incorporated in the model developed by Schultheiss (2003). The remaining model parameters, listed in Table 3.1 were left unchanged.

Note that Schultheiss' model was set up to use a simplified description of the moment-rotation profile of the hinges, and most of his simulations assumed the moment to remain constant at each hinge. In order to provide a more realistic description of the moment-rotation profiles, based on the experimental tests, piece-wise linear profiles were used, described by the values listed in Table 3.2. More accurate piece-wise linear relationships, described by larger numbers of points could not be used due to convergence problems.

The latching times predicted by this analysis are listed in Table 3.3, alongside the average times measured by Schultheiss. It can be seen that the order in which the three hinges latch is predicted correctly, with the predicted latching times being shorter than those found experimentally.

Parameter	Symbol	Value	Units
Mass Panel 1	$M1$	0.984	kg
Mass Panel 2	$M2$	4.618	kg
Mass Panel 3	$M3$	4.530	kg
Mass Hinge Line	Mh	0.0612	kg
Length Panel 1	$L1$	0.5	m
Length Panel 2	$L2$	1.2	m
Length Panel 3	$L3$	1.2	m
Separation of panels	sp	0.083	m
Mass transverse trolley	mt	0.117	kg
Mass trans. tube + long. trolleys	mr	1.275	kg
Longitudinal friction	μx	0.001	-
Transverse friction	μy	0.001	-
Pusher spring energy	$epot$	0.18	J

Table 3.1: Parameters for Schultheiss (2003) deployment test.

Root Hinge		Panel-Panel Hinge	
Rotation (deg)	Moment (Nmm)	Rotation (deg)	Moment (Nmm)
0	0	0	0
2	900	2	6000
10	310	2.2	2400
12	200	8	1060
62	200	16.28	277
90	273	24.8	177
-	-	60.4	215
-	-	112.8	85
-	-	124	0
-	-	180	0.15

Table 3.2: Piecewise-linear moment-rotation profiles used in deployment analysis.

Latch event	Experimental		Analytical	
	Time (s)	Hinge	Time (s)	Hinge
1	6.9	H1	4.75	H1
2	11.03	H3	10.01	H3
3	12.89	H2	12.31	H2

Table 3.3: Experimental and analytical latching times.

These differences could be due to air drag, errors in the measurement of hinge moments, or differences between the analytical model and the experiment due to various simplifying assumptions.

For example, one of the simplifications is the assumption that in the model the tape-spring hinges are represented by a single revolute joint lying in the mid-plane of the panels and at a distance of 40 mm from either end. In reality, a tape-spring hinge has no fixed center of revolution. Another simplification is that in the deployment experiments carried out by Schultheiss the tape-springs were not folded in the configuration of lowest strain energy, as they were in the moment-rotation test. This will somewhat alter the deployment behaviour.

3.1.1 Sensitivity to Friction

The effects of friction in the bearings, already investigated by Schultheiss (2003), were further investigated using the updated hinge moment-rotation profiles. The values of friction in the longitudinal and transverse trolleys, represented by the friction coefficients $\mu_x = \mu_y$, were varied.

It was found that the order in which the hinges latch is not affected, but the timings of each latching vary as shown in Table 3.4. It can be seen that increasing the value of μ increases all of the latching times, but has a greater effect on the later latching times than the earlier ones. As the largest discrepancy between the analytical and experimental results in Table 3.3 was in the time for the first latching to occur, it seems unlikely that the discrepancy is due to an incorrect value for the friction coefficient being used in the simulation.

Latch event	Hinge	$\mu = 0$	$\mu = 0.001$	$\mu = 0.0015$	$\mu = 0.002$
1	H1	4.39	4.75	4.96	5.24
2	H3	9.19	10.01	10.62	11.48
3	H2	10.08	12.31	13.41	14.75

Table 3.4: Sensitivity of predicted latching times to changes in friction.

3.1.2 Sensitivity to Horizontality of Longitudinal Tubes

The longitudinal tubes of the gravity offload system need to be horizontal, otherwise additional deployment forces due to gravity will arise. It is important to establish what level of horizontal misalignment can be tolerated without significant effects on the results of a deployment experiment.

The effect of a misalignment of the main longitudinal tubes of the fixed support frame can be included in the deployment model simply by modifying the longitudinal friction. As the trolleys that run on these tubes move only longitudinally, without ever reversing the sense of motion, a slope in the tube can be modelled by changing the longitudinal friction coefficient. The modified friction coefficient is given by

$$\mu_{x\prime} = \mu_x - \tan(\theta) \tag{3.1}$$

where θ is the angle (in radians) between the tube and the horizontal, and a positive angle corresponds to the end of the longitudinal tubes near the root hinge being higher than the other end. For small misalignment angles Equation 3.1 simplifies to

$$\mu_{x\prime} = \mu_x - \theta \tag{3.2}$$

The effects of varying θ can be understood from Table 3.5, where it is assumed that $\mu_x = \mu_y = 0.0001$ throughout.

Latch	$\theta = 0$	$\theta = 0.001$	$\theta = -0.001$	$\theta = 0.0001$	$\theta = 0.0005$
1	4.75	4.5 (-3.8)	4.98 (4.8)	4.72 (-0.6)	4.62 (-2.7)
2	10.01	9.19 (-8.2)	11.33 (13.1)	9.92 (-0.9)	9.58 (-4.3)
3	12.31	10.25 (-16.7)	14.97 (21.6)	12.08 (-1.9)	11.21 (-8.9)

Table 3.5: Sensitivity of latching times, in seconds (percentage difference in brackets), to slope of longitudinal tubes, θ in radians.

It can be seen that the deployment is very sensitive to the horizontality of the longitudinal tubes. Even a misalignment angle as small as $\theta = 0.0001$, i.e. a 0.1 mm change in height for every 1 m length of tube, changes the time for the third latching by nearly 2%. This suggests that great care will be needed in levelling the longitudinal tubes.

The horizontality of the transverse tubes will also be important, but the effects of misalignment in these tubes will be harder to predict due to the changing direction of travel of the transverse trolleys during deployment. Hence, a simple change in the coefficient of friction cannot be used to analyse this effect.

3.2 Simulation with Pro/Mechanica

To use the full hinge moment-rotation profiles and to possibly include in future air drag forces in the simulation, a Pro/Mechanica (PTC, 2003) model of the solar array wing and gravity offload system was set up. This model is also able to analyse the maximum moments induced by latching.

The Pro/Mechanica model, shown in Figure 3.1, consists of three rigid panels —representing the yoke plus two solar panels— and the gravity compensation system. The root hinge is modelled by a revolute hinge and the panel-panel hinges are modelled by revolute joints at a distance of 40 mm from the edge of the panels. Revolute joints connect the second and third panels to hangers, which are connected via sliders in the y-direction to the lateral tubes. These are in turn connected to the longitudinal tubes by a slider in the x-direction. This model uses the same parameters as the Schultheiss model, see Table 3.1, and hence exactly the same values were given to the panel length, mass, moment of inertia, etc.

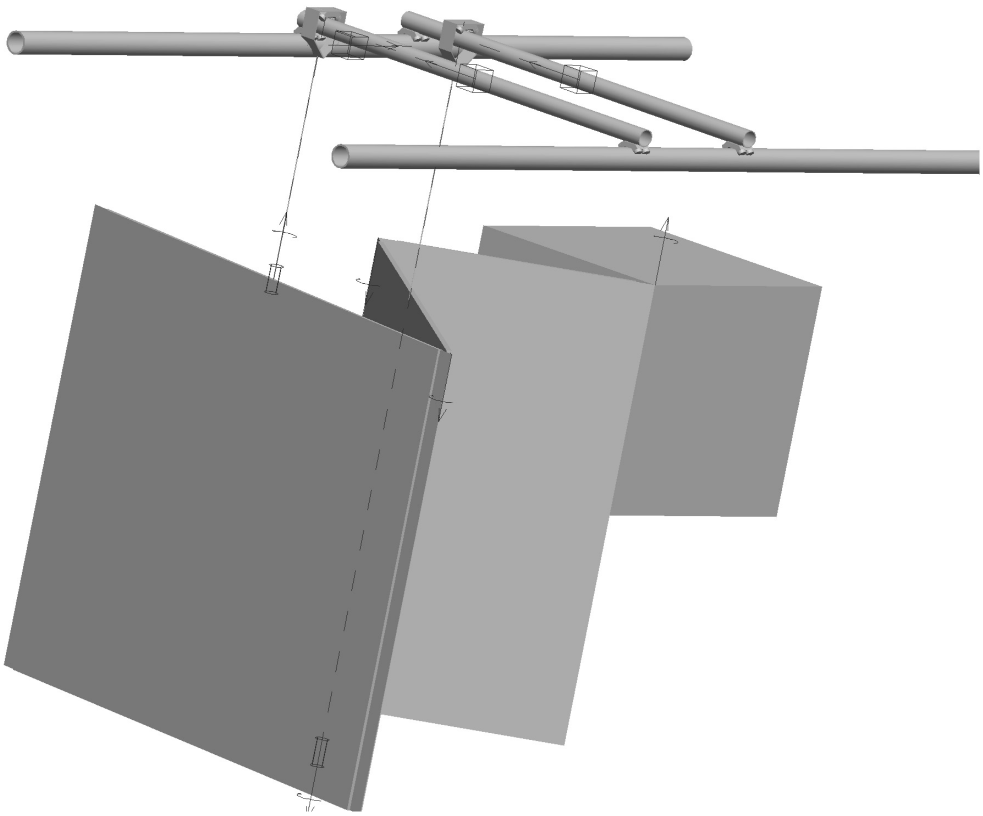

Figure 3.1: Pro/Mechanica deployment model.

3.2.1 Model Details

Graphical representations of the root-hinge and panel-panel moment profiles (based on our experimental measurements) are given in Figure 3.2. The numerical values that define each line in this plot are listed in Table 3.6.

Here, the angles of the hinges are defined to be 0° in the fully folded configuration. The rotations, and hence the velocities ω_i, are positive in the sense in which deployment occurs. Therefore, the fully deployed configuration corresponds to 90° for the root hinge and 180° for the panel-panel hinge.

Latching of a hinge is modelled by applying large, linearly varying moments when the hinge goes beyond its the deployed configuration. Then, when the latched hinge unloads elastically and reaches its maximum rebound rotation the moment is reset to the deployment value. This discontinuity results in a sudden loss of strain energy and is very effective in damping the post-latching vibration of the panel.

In the folded configuration all hinge rotations are initially zero, and they are prevented from becoming negative (corresponding to the panels colliding with each other) by applying large deployment moments for negative rotations.

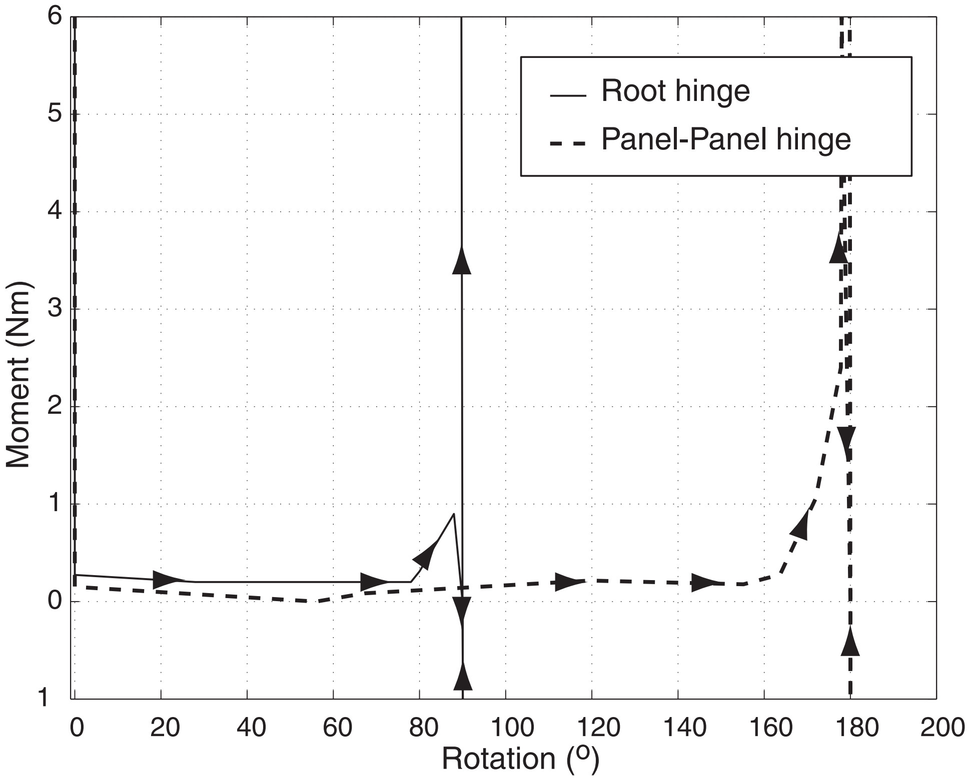

Figure 3.2: Plot of moment versus rotation for root hinge and panel-panel hinge.

Moment	M1	M1R	M2	M2R	M3	M3R	M3Neg
Hinge	H1	H1	H2	H2	H3	H3	H3
Condition	$\omega_1 \geq 0$	$\omega_1 < 0$	$\omega_2 \geq 0$	$\omega_2 < 0$	$\omega_3 \geq 0$	$\omega_3 < 0$	$\theta_3 < 0$
-0.001	-	-	-	-	-	-	1.75E+12
0.0	0.273	-	0.15	-	0.15	-	0
28.00	0.2	-	-	-	-	-	-
56.0	-	-	0	-	0	-	-
67.2	-	-	0.085	-	0.085	-	-
78.00	0.2	-	-	-	-	-	-
80.00	0.31	209	-	-	-	-	-
88.00	0.9	-	-	-	-	-	-
90.00	0	0	-	-	-	-	-
100.00	-209	-209	-	-	-	-	-
119.6	-	-	0.215	-	0.215	-	-
155.2	-	-	0.177	-	0.177	-	-
163.7	-	-	0.277	-	0.277	-	-
170.0	-	-	-	400	-	400	-
172.0	-	-	1.06	-	1.06	-	-
177.8	-	-	2.4	-	2.4	-	-
178.0	-	-	6	-	6	-	-
180.0	-	-	0	0	0	0	-
190.0	-	-	-400	-400	-400	-400	-

Table 3.6: Moments applied in Pro/Mechanica model (units: Nm, degrees).

In addition to the moments described above, a pusher spring force and a force preventing the panels from having a negative displacement in the x-direction are included. The pusher spring applied a constant force of 50 N, acting over a distance of 3.6 mm and hence giving a total energy input to the system of 0.18 J. When a negative displacement occurs (i.e., the x-direction component of displacement of the end of panel two becomes negative) a force, linearly increasing with displacement, is applied.

Latch Event	Analytical	Pro/Mechanica
1	4.75	4.8
2	10.01	10.0
3	12.31	11.8

Table 3.7: Latching times from Schultheiss and Pro/Mechanica models (s).

Table 3.7 compares the latching times predicted by this Pro/Mechanica analysis to those found from the Schulthess model (analytical). It can be seen that the first and second latching have very similar times (less than 2% difference), while there is a slight difference in the time for the third latching ($\approx$ 5% difference).

3.2.2 Latching Shocks

The Pro/Mechanica model was used to investigate the magnitude of the latching shocks arising at the root hinge. These shocks are of importance in determining the loading on the SADM and will determine whether additional compliance will be needed.

Because of the way that the Pro/Mechanica model was set up, finding the latching shock is simply a matter of querying the total load applied at the root hinge. However, care has to be taken in ensuring that the output time step used in the analysis is sufficiently small that the peak moment applied by the hinge is captured.

This analysis was made for the case where the solar array wing deploys in space, and hence both the mass and inertia of the gravity compensation system and the friction it introduces were removed. The results of this analysis can be seen in Table 3.8; notice that larger moments were captured as the integration time step was reduced.

The maximum shock at the root hinge occurs during latching of the first hinge.

The maximum axial and radial loading on the root hinge are also found from the simulation, by looking at the reactions at the root hinge connection. These loads are 46 N and 73 N respectively, again both occurring during the first latching.

Output Time Step (s)	0.1	0.01	0.002
Max Moment (Nm)	33.07	40.15	40.82
Time (s)	4.2	4.24	4.34

Table 3.8: Maximum moments at root hinge during deployment.

Chapter 4

Air Drag Effects

4.1 Experimental Analysis of Effects of Air Drag

The effect of air drag on the deployment of the solar array wing has not been included in any of the analyses. In order to investigate the validity of this approximation through an indirect measurement of the magnitude of the effects of air drag, an experiment was carried out.

The experiment consisted in comparing the latching times for the deployment of the standard array wing set-up, described in Section 4.2 of Schultheiss (2003) —shown in Figure 4.1— with latching times measured when the holes in the panels are covered. Covering these holes increases the area of the panels, the root panel increasing in area by about a third —from 0.15 m^2 to 0.21 m^2— and the second and third panels more than doubling their area, from roughly 0.41 m^2 to 0.84 m^2.

These area increases have the effect of approximately doubling the air drag and will therefore give an indication as to whether air drag has a significant effect on the latching times.

The latching times resulting from a series of experiments, for the case when the panels are covered or left uncovered, are listed in Table 4.1. The mean and standard deviation of the latching times are given in Table 4.2.

		panels uncovered					panels covered		
Test No.	Hinge	1	2	3	4	5	6	7	8
Latch 1	H1	6.9	6.2	6.3	7	6.6	6.5	6.6	6.6
Latch 2	H3	11.2	10.8	10.9	11.1	11.2	11.0	11.4	11.5
Latch 3	H2	16.1	15.6	16.3	15.1	15.8	14.4	14.5	14.7

Table 4.1: Latching times (s) for panel deployments.

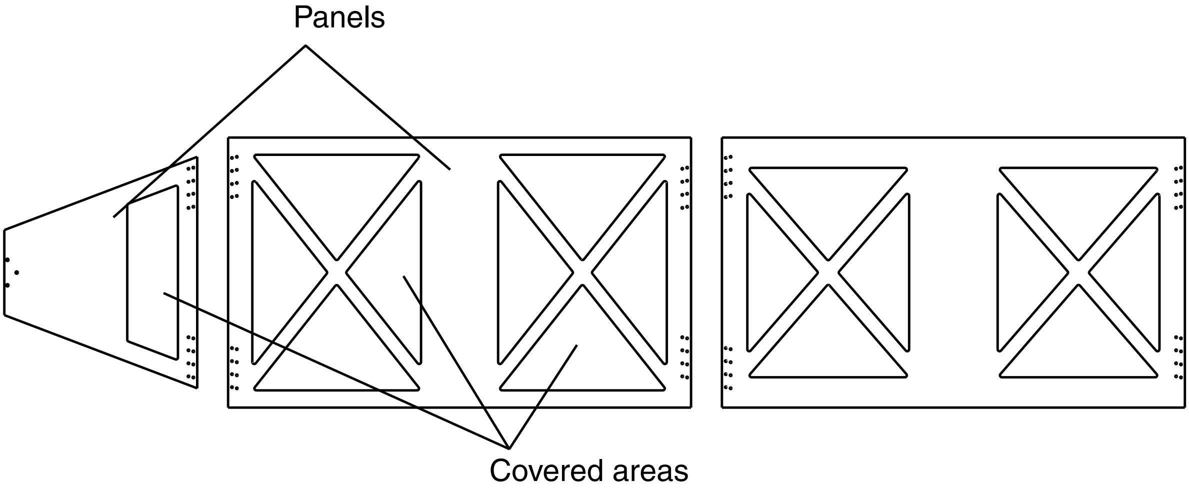

Figure 4.1: SSTL Array deployment set-up – covered areas.

	uncovered		covered	
	Time	S.D	Time	S.D.
Latch 1	6.6	0.3	6.6	0.1
Latch 2	11.0	0.2	11.3	0.2
Latch 3	15.8	0.5	14.5	0.1

Table 4.2: Mean and standard deviations of latching times (s).

Note that a new set of tests on the uncovered panel system was carried out, rather than relying on the results from Schultheiss (2003), as several months had elapsed since Schultheiss' tests had been completed, and there may have been some misalignments introduced during this period.

Based on the results presented in Table 4.2, it can be concluded that the effect of the additional air drag introduced by covering the panels is rather small, the average latching times having a maximum difference of less than eight percent. These small differences are practically of the same order as the experimental variability in the latching times, which suggests that air drag effects on the panels are small.

The average time for the first latching remained practically unchanged when the panels were covered. However, interestingly, the individual test results in Table 4.1 —although only a relatively small sample— suggest that the latching times for the first panel were more consistent with the panels covered. This result could be explained by a more consistent transfer of energy from the pusher spring.

Chapter 5

Conclusion

5.1 Discussion of Moment-Rotation Relationships

The moment-rotation relationship of both panel-panel hinge and root hinge has been shown to be predictable with good accuracy by means of a non-linear finite-element analysis. These predictions are particularly accurate for the panel-panel hinge.

An important effect that has been observed is that the deployment moment of a panel-panel hinge, that is allowed to start unfolding from its least energy configuration, becomes zero over a small range of rotation angles. However, our simulations show that the moment remains positive throughout deployment if the ends of the hinge are initially pushed closer together (as it is envisaged in the folded configuration of the SSTL array).

In the case of the root hinge, experimentally measured moments are about 30% lower than the finite element predictions. Based on observations made while developing the current model, it is possible that more accurate predictions would be obtained by using a finer mesh of finite elements.

In the experiments, the ends of the panel-panel hinge did not come as close to each other as in the SSTL array, because this would have required the two ends to be pushed towards one another. While the simulation of a hinge —whose fully-folded configuration matches the experimental conditions— closely follows the measured response, a concerning feature of this response is that the moment is predicted —and indeed also experimentally observed— to become zero at a rotation of about 130°. The simulation of a hinge with the actual separation that will occur in the array shows the deployment moment to remain positive throughout, but this result has yet to be verified experimentally.

5.2 Discussion of Deployment Simulations

The revised analysis of Schultheiss' deployment experiments has shown that the analytical model predicts all hinge latchings to occur earlier than measured experimentally. The discrepancy is significant, 31%, for the first hinge but decreases to 10% and 4%, respectively, for the second and third latchings.

Air effects, not included in the model, are unlikely to be the main reason for these discrepancies. As it has been shown that even a small misalignment in the gravity offload longitudinal tubes can affect significantly the hinge latching times, it is important to quantify this misalignment in future work and possibly include its effects in a revised model.

Acknowledgments

The research presented in this report was funded by a research contract between Surrey Satellite Technology Ltd (SSTL) and the University of Cambridge.

The authors are grateful to Paul Charman, Karel Jacobs, and Guy Richardson for technical support and advice.

References

ABAQUS (2002). Abaqus Version 6.3. Pawtucket, RI 02860.

Calladine, C. R. (1988). The theory of thin shell structures 1888-1988. Proceedings of the Institution of Mechanical Engineers202, 1-9.

Fischer, A. (1995). Bending instabilities of thin-walled transversely curved metallic springs, Department of Engineering, University of Cambridge, Technical Report CUED/D-STRUCT/ TR154.

Givois, D., Sicre, J. and Mazoyer, T. (2001). A Low Cost Hinge for Appendices Deployment: Design, Test and Applications. 9th European Space Mechanisms and Tribology Symposium, 19-21 September 2001, Liege, Belgium.

PTC (2003). Pro/Mechanica Wildfire, Version 1.

Schultheiss, D. (2003). Gravity compensation of deployable solar arrays for small spacecraft, Department of Engineering, University of Cambridge, Technical Report CUED/D-STRUCT/ TR210.

Appendix A

Drawings of Hinge Components

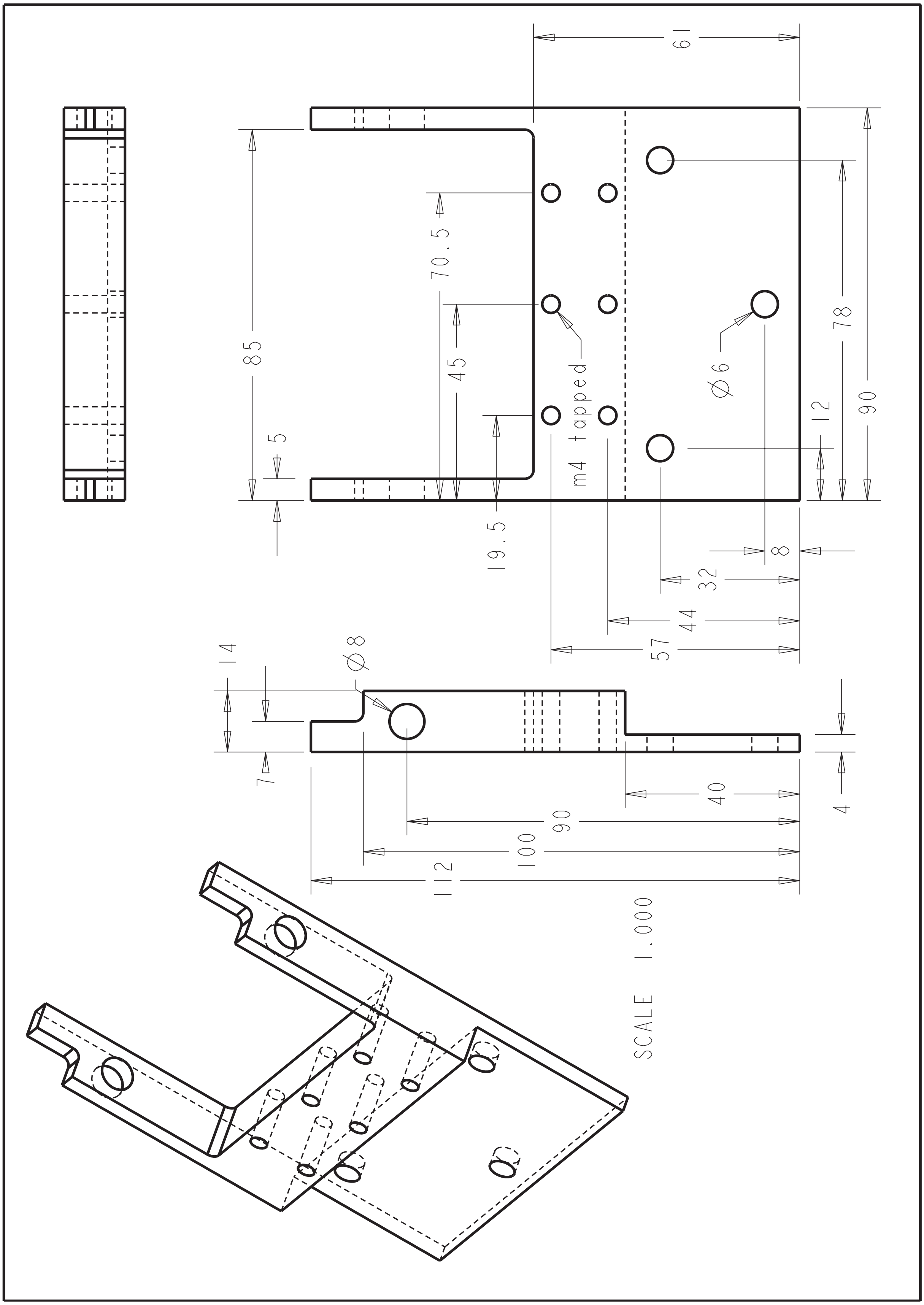

Figure A.1: Root hinge Body 1.

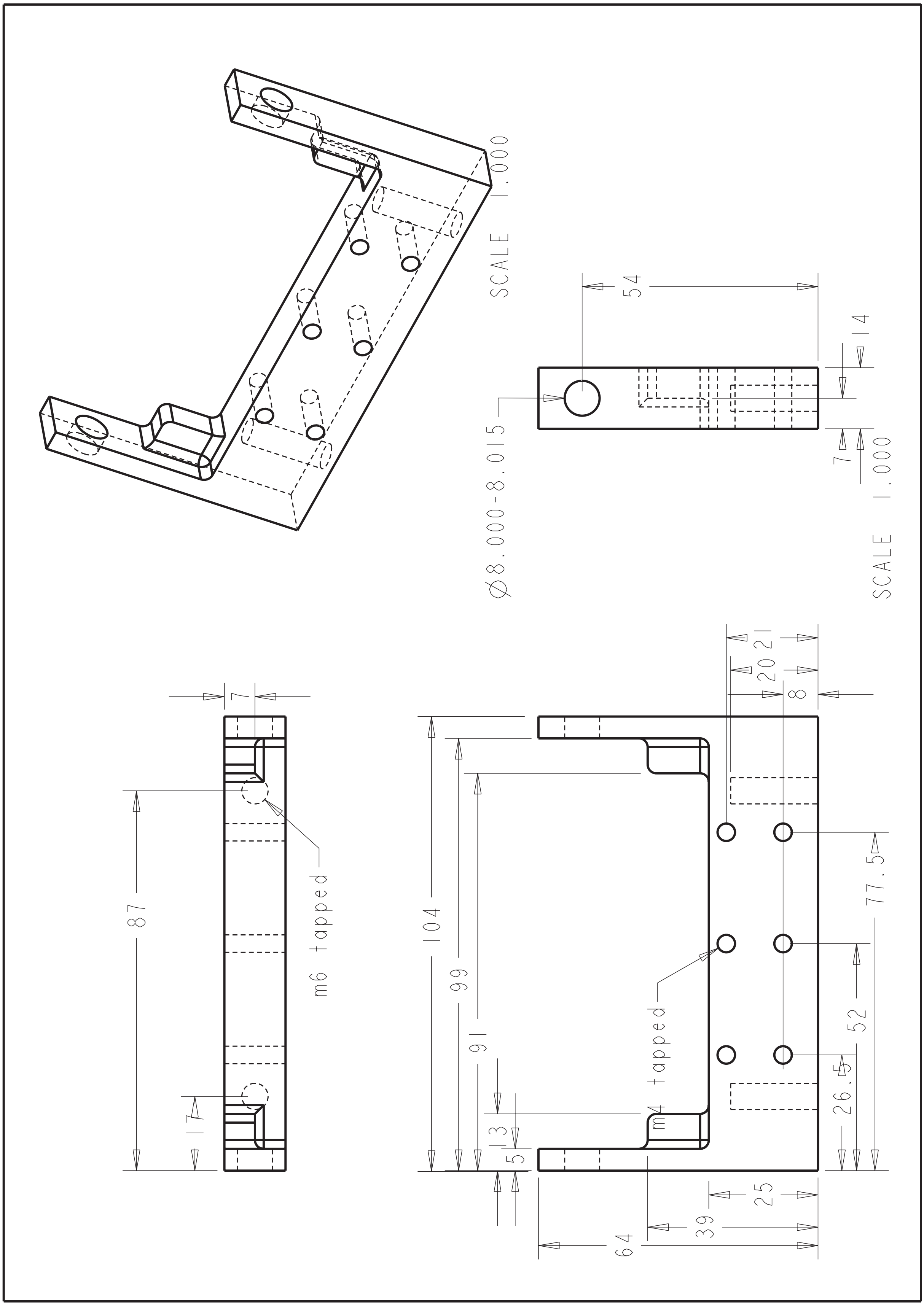

Figure A.2: Root hinge Body 2.

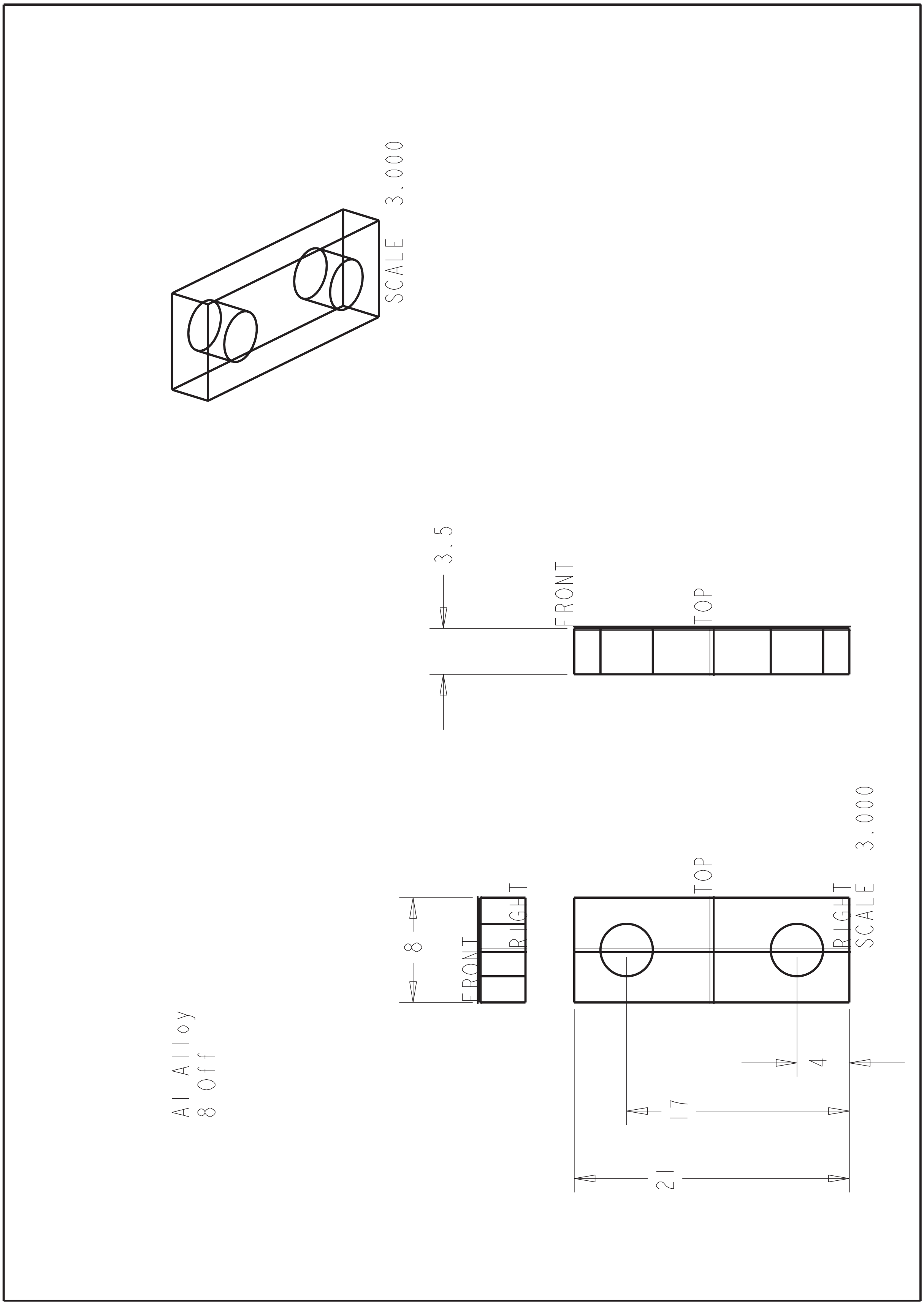

Figure A.3: Root hinge spacer.

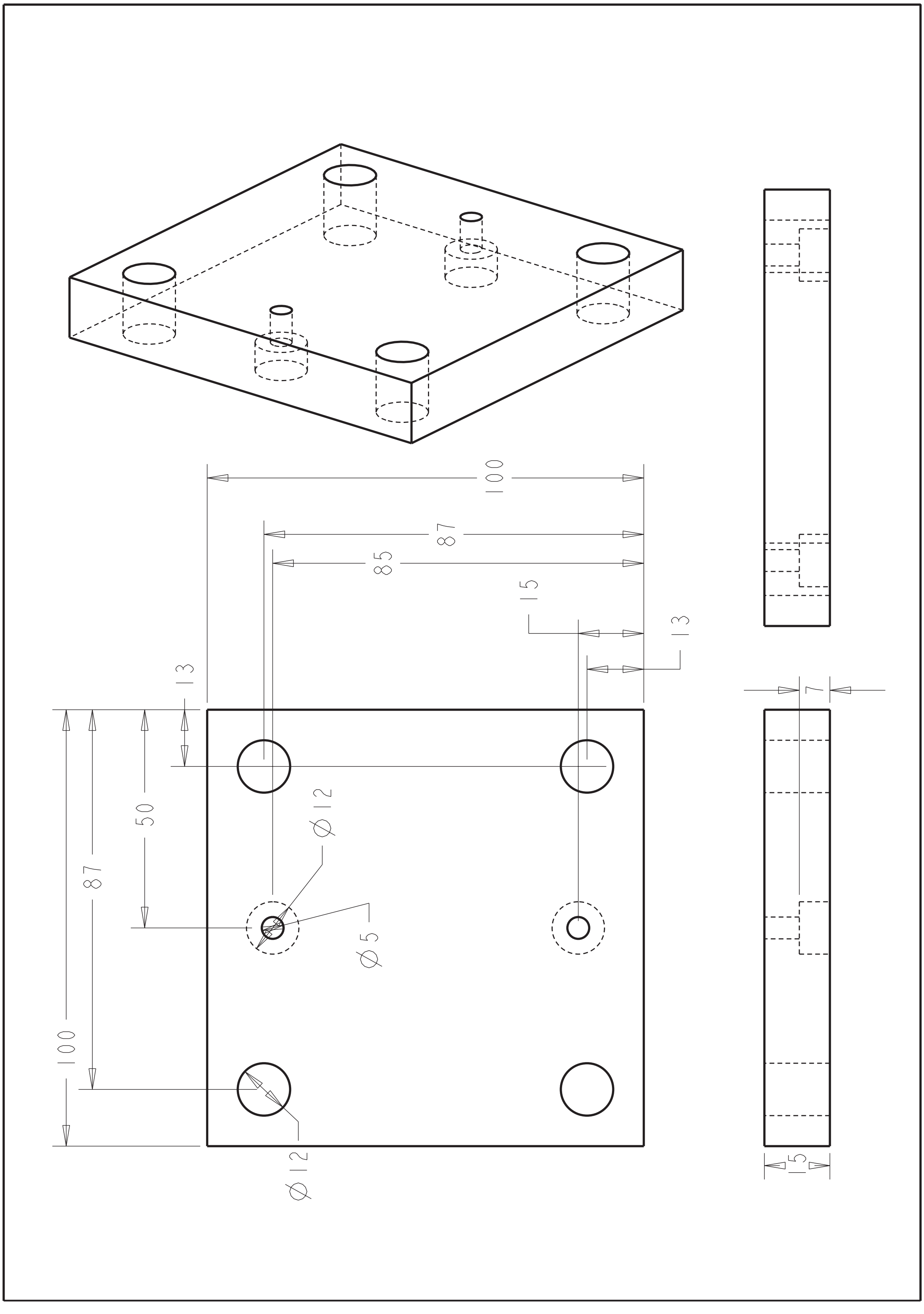

Figure A.4: Root hinge to scaffolding connector.

Appendix B

Finite Element Models

B.1 Panel-Panel Tape-Spring Folding Model

```
*HEADING
****************************
** PANEL-PANEL TAPE HINGE **
****************************
**
*PREPRINT, ECHO=NO, HISTORY=NO, MODEL=NO
**
**************************************
** DEFINING THE NODES FOR THE TAPES **
**************************************
*NODE
1,-26.585,-65.785,7.901
2,-24.883,-66.165,8.879
3,-23.181,-66.546,9.858....
...1663,26.585,65.785,-7.901
*******
*NSET, NSET=TOP_FRONT, GENERATE
1,13,1
*NSET, NSET=TOP_BACK, GENERATE
651,663,1
*NSET, NSET=TOP_LEFT, GENERATE
```

```
1,651,13
*NSET, NSET=TOP_RIGHT, GENERATE
13,663,13
**
**
*NSET, NSET=BOTTOM_FRONT, GENERATE
1001,1013,1
*NSET, NSET=BOTTOM_BACK, GENERATE
1651,1663,1
*NSET, NSET=BOTTOM_LEFT, GENERATE
1001,1651,13
*NSET, NSET=BOTTOM_RIGHT, GENERATE
1013,1663,13
**
**
*NSET, NSET=TOP_TAPE_N, GENERATE
1,663,1
*NSET, NSET=BOTTOM_TAPE_N, GENERATE
1001,1663,1
*NSET, NSET=TAPES_N
TOP_TAPE_N,BOTTOM_TAPE_N
******************************************
**CREATING SHELL ELEMENTS FOR THE TAPES **
******************************************
**
*ELEMENT, TYPE=S4
1, 1, 14, 15, 2
*ELGEN, ELSET=TOP_TAPE_EL
1, 12, 1, 1, 50, 13, 12
**
*ELEMENT, TYPE=S4
1001, 1001, 1014, 1015, 1002
*ELGEN, ELSET=BOTTOM_TAPE_EL
```

```
1001, 12, 1, 1, 50, 13, 12
*ELSET, ELSET=TAPES_EL
TOP_TAPE_EL,BOTTOM_TAPE_EL
************************
** MATERIAL PROPERTIES**
************************
**
*MATERIAL, NAME=STEEL
*ELASTIC, TYPE=ISO
200000, 0.3
*******************
** SHELL SECTION **
*******************
*SHELL SECTION, ELSET=TOP_TAPE_EL, MATERIAL=STEEL
0.115, 5
**
*SHELL SECTION, ELSET=BOTTOM_TAPE_EL, MATERIAL=STEEL
0.115, 5
*****************************
** NODES WITHIN THE CLAMPS **
*****************************
**
*NSET, NSET=FRONT_CLAMP
5,18,31,44,6,19,32,45,7,20,33,46,8,21,34,47
9,22,35,48,1005,1018,1031,1044,1006,1019,1032,1045,1007,1020
1033,1046,1008,1021,1034,1047,1009,1022,1035,1048
*NSET, NSET=BACK_CLAMP
616,629,642,655,617,630,643,656,618,631,644,657,619,632,645,658
620,633,646,659,1616,1629,1642,1655,1617,1630,1643,1656,1618
1631,1644,1657,1619,1632,1645,1658,1620,1633,1646,1659
**********************************************
** NODES AND THE ELEMENTS FOR THE RIGID ARM **
**********************************************
```

```
*NODE, NSET=FRONT_ARM_N
2000,0,-18,-5
***
*NODE, NSET=BACK_ARM_N
3000,0,18,-5
**************************************************************
** KINEMATIC COUPLING BETWEEN THE CLAMPS AND THE RIGID ARMS **
**************************************************************
**
*KINEMATIC COUPLING, REF NODE=2000
FRONT_CLAMP, 1,6
*KINEMATIC COUPLING, REF NODE=3000
BACK_CLAMP, 1,6
**************
** ANALYSIS **
**************
**
*STEP, INC=1000, NLGEOM
Folding
*STATIC,STABILIZE,FACTOR=0.0001
0.0001, 1, 1.E-30
**
*BOUNDARY
2000,1,3
2000,5,6
3000,1,3
3000,5,6
*BOUNDARY
2000, 4,, -1.570796
3000, 4,, 1.570796
**
*CONTROLS, ANALYSIS=DISCONTINUOUS
***CONTROLS, PARAMETER=TIME INCREMENTATION
```

```
** 20,18,,,,,,20,
**
*RESTART, WRITE, OVERLAY
**
*NODE PRINT, NSET=TAPES_N, FREQUENCY=1
U
*END STEP
```

B.2 Panel-Panel Unfolding Model

```
*HEADING

*RESTART, READ, END STEP,STEP=1,INC=181

**

*STEP, INC=1000, NLGEOM

coords:

*STATIC,STABILIZE,FACTOR=1e-8

0.00001, 1, 1.E-30,0.02

*BOUNDARY, OP=NEW

2000, 1, 3

2000,5,6

3000, 1

3000, 3

3000,5,6

2000, 4,, 0

3000, 4,, 0

**

*RESTART, WRITE, OVERLAY

**

*NODE PRINT, NSET=FRONT_ARM_N, FREQUENCY=1

RF

*NODE PRINT, NSET=BACK_ARM_N, FREQUENCY=1

RF

*END STEP
```

B.3 Root Hinge Folding Model

```
*HEADING
****************
** TAPE HINGE **
****************
*PREPRINT, ECHO=NO, HISTORY=NO, MODEL=NO
**************************************
** DEFINING THE NODES FOR THE TAPES **
**************************************
*NODE
   1,-11.5944,-50,10.0006
   2,-9.8502,-50,10.9794
   3,-8.1061,-50,11.9581
   4,-6.3620,-50,12.9396
   5,-4.4462,-50,13.8160
   6,-2.2574,-50,14.4025...
   ... 1307,0,50,14.6
   1308,2.2574,50,14.4025
   1309,4.4462,50,13.8160
   1310,6.3620,50,12.9396
   1311,8.1061,50,11.9581
   1312,9.8502,50,10.9794
   1313,11.5944,50,10.0006
*******
*NSET, NSET=TOP_FRONT, GENERATE
1,13,1
*NSET, NSET=TOP_BACK, GENERATE
1301,1313,1
*NSET, NSET=TOP_LEFT, GENERATE
1,1301,13
*NSET, NSET=TOP_RIGHT, GENERATE
13,1313,13
 *NSET, NSET=TOP_TAPE_N, GENERATE
```

```
 1,1313,1
*NSET, NSET=TAPES_N TOP_TAPE_N
******************************************
**CREATING SHELL ELEMENTS FOR THE TAPES **
******************************************
*ELEMENT, TYPE=S4
1, 1, 14, 15, 2
*ELGEN, ELSET=TOP_TAPE_EL
1, 12, 1, 1, 100, 13, 12
************************
** MATERIAL PROPERTIES**
************************
*MATERIAL, NAME=STEEL
*ELASTIC, TYPE=ISO
200000, 0.3
*******************
** SHELL SECTION **
*******************
*SHELL SECTION, ELSET=TOP_TAPE_EL, MATERIAL=STEEL
0.115, 5
*****************************
** NODES WITHIN THE CLAMPS **
*****************************
*NSET, NSET=FRONT_CLAMP
5,6,7,8,9,18,19,20,21,22,31,32,33,34,35,44,45,46,47,48,57,58,59,60,61,70,
71,72,73,74,83,84,85,86,87,96,97,98,99,100,109,110,111,112,113,122,123,124,
125,126,135,136,137,138,139,148,149,150,151,152,161,162,163,164,165,174,175,176,
177,178,187,188,189,190,191,200,201,202,203,204,213,214,215,216,217,226,227,228,
229,230,239,240,241,242,243,252,253,254,255,256,265,266,267,268,269,278,279,280,
281,282,
*NSET, NSET=BACK_CLAMP
1032,1033,1034,1035,1036,1045,1046,1047,1048,1049,1058,1059,1060,1061,1062,
1071,1072,1073,1074,1075,1084,1085,1086,1087,1088,1097,1098,1099,1100,1101,
```

```
1110,1111,1112,1113,1114,1123,1124,1125,1126,1127,1136,1137,1138,1139,1140,
1149,1150,1151,1152,1153,1162,1163,1164,1165,1166,1175,1176,1177,1178,1179
1188,1189,1190,1191,1192,1201,1202,1203,1204,1205,1214,1215,1216,1217,1218,
1227,1228,1229,1230,1231,1240,1241,1242,1243,1244,1253,1254,1255,1256,1257,
1266,1267,1268,1269,1270,1279,1280,1281,1282,1283,1292,1293,1294,1295,1296,
1305,1306,1307,1308,1309
**********************************************
** NODES AND THE ELEMENTS FOR THE RIGID ARM **
**********************************************
*NODE, NSET=FRONT_ARM_N 2000,0,0,0.6
*NODE, NSET=BACK_ARM_N
3000,0,0,0.6
**************************************************************
** KINEMATIC COUPLING BETWEEN THE CLAMPS AND THE RIGID ARMS **
**************************************************************
*KINEMATIC COUPLING, REF NODE=2000
FRONT_CLAMP, 1,6
*KINEMATIC COUPLING, REF NODE=3000
BACK_CLAMP, 1,6
**************
** ANALYSIS **
**************
*STEP, INC=1000, NLGEOM
Folding
*STATIC,STABILIZE,FACTOR=1e-6
0.0001, 1, 1.E-30
*BOUNDARY
2000,1,3
2000,5,6
3000,1,3
3000,5,6
*BOUNDARY
2000, 4,, -0.785398
```

```
3000, 4,, 0.785398

*CONTROLS, ANALYSIS=DISCONTINUOUS

*CONTROLS, PARAMETER=TIME INCREMENTATION 20,18,,,,,,20,

*RESTART, WRITE, OVERLAY

*NODE PRINT, NSET=FRONT_ARM_N, FREQUENCY=1 RM1

*END STEP
```

Appendix C

Measurements of Moment-Rotation Profiles

Root hinge		Panel-Panel Hinge			
Rotation	Moment	Rotation	Moment	Rotation	Moment
°	Nmm	°	Nmm	°	Nmm
90	273	180	240	180	218
87	236	171	233	171	187
81	242	162	209	162	200
77	225	153	182	153	108
73	212	144	141	144	134
68	208	135	68	135	53
63	202	126	32	126	-45
59	207	117	159	117	151
54	201	108	130	108	136
51	192	99	140	99	124
47	203	90	153	90	140
42	191	81	159	81	145
38	190	72	174	72	149
33	183	63	212	63	153
29	185	54	308	54	175
26	180	45	381	45	227
21	196	36	403	36	390
17	206	27	442	27	431
13	214	18	568	18	604
9	311	-	-	-	-

Table C.1: Experimental moment rotation results for root hinge and panel-panel hinge (two experiments).